Li et al. *Microsystems & Nanoengineering* (2025)11:65
https://doi.org/10.1038/s41378-025-00916-4

Microsystems & Nanoengineering
www.nature.com/micronano

ARTICLE Open Access

Extracellular vesicle-based point-of-care testing for diagnosis and monitoring of Alzheimer's disease

Xiang Li[1], Jie Chen[2], Yang Yang[1,3], Hongwei Cai[1], Zheng Ao[1], Yantao Xing[1], Kangle Li[1], Kaiyuan Yang[1], Weihua Guan[1], James Friend[4], Luke P. Lee[3,5,6,7]✉, Nian Wang[2]✉ and Feng Guo[1]✉

Abstract

Extracellular vesicles (EVs) show potential for early diagnosis of Alzheimer's disease (AD) and monitoring of its progression. However, EV-based AD diagnosis faces challenges due to the small size and low abundance of biomarkers. Here, we report a fully integrated organic electrochemical transistor (OECT) sensor for ultrafast, accurate, and convenient point-of-care testing (POCT) of serum EVs from AD patients. By utilizing acoustoelectric enrichment, the EVs can be quickly propelled, significantly enriched, and specifically bound to the OECT detection area, achieving a gain of over 280 times response in 30 s. The integrated POCT sensor can detect serum EVs from AD patients with a limit of detection as low as 500 EV particles/mL and a reduced detection time of just two minutes. Furthermore, the integrated POCT sensors were used to monitor AD progression in an AD mouse model by testing the mouse Aβ EVs at different time courses (up to 18 months) and compared with the Aβ accumulation using high-resolution magnetic resonance imaging (MRI). This innovative technology has the potential for accurate and rapid diagnosis of Alzheimer's and other neurodegenerative diseases, and monitoring of disease progression and treatment response.

Alzheimer's disease (AD) is a progressive neurodegenerative disease representing the main cause of dementia[1]. The presence of amyloid β(Aβ)-containing plaques and tau-containing neurofibrillary tangles in the brain tissues are two hallmark signs of AD[2]. Targeting these characteristics, current neuroimaging methods such as magnetic resonance imaging (MRI) are used to accurately determine the underlying etiology of AD. MRI-based AD detection is safe, convenient, and non-invasive, but may lack the sensitivity to diagnose AD at very early stages[1,3]. Recently, the blood-based Aβ and tau molecules have been considered promising AD biomarkers and have been developed for AD detection[4]. However, their sensitivity and specificity still limit their clinical applications due to the low abundance of these proteins and the complex composition of clinical samples. Extracellular vesicles (EVs) are nano/microscale membrane-enclosed vesicles secreted by cells[5,6], and highly abundant in various biofluids including blood and cerebrospinal fluid[7]. Importantly, EVs isolated from AD patient blood samples are tested to carry membrane Aβ and tau proteins as well as AD-related mRNA and microRNAs[8,9] and may provide an alternative means for AD detection[10,11]. However, challenges remain in early diagnosis and progression monitoring of AD by sensing EVs from individual patients due to their small size (typically 50 ~ 200 nm in diameter) and high heterogeneity[12–15].

To address the challenges in personalized diagnosis, point-of-care testing (POCT) technology has been developed[13,16–18]. Along the high sensitivity and specificity, the technology may enable the "bench to bedside" EV-based AD diagnosis with several unique features simultaneously: (1) short turnaround time, as it should have the ability to detect EVs in minutes; (2) ease of use, as patients can easily use it after reading some simple instructions; (3) compatibility, as it must have the ability to test simply handled samples; and (4) low cost, as an important basis for rapid adoption and broad use. By converting

Correspondence: Luke P. Lee (lplee@bwh.harvard.edu) or
Nian Wang (Nian.Wang@UTSouthwestern.edu) or
Feng Guo (fengguo@iu.edu)
[1]Department of Intelligent Systems Engineering, Indiana University, Bloomington, IN 47405, USA
[2]Advanced Imaging Research Center, University of Texas Southwestern Medical Center, Dallas, TX 75390, USA
Full list of author information is available at the end of the article
These authors contributed equally: Xiang Li, Jie Chen, Yang Yang.

biomolecular fingerprints into electrical signals, an organic electrochemical transistor (OECT) emerges as an excellent sensor with a microscale footprint for various POCT applications[19–27]. In the conventional OECT measurements, the target analytes (e.g., EVs) rely on the slow and random diffusion to specifically bind to the sensing region, which limits the detection limitation and is also time-consuming especially when handling with patient serum or blood samples at a small volume[28]. Thus, the rapid enrichment of EVs to the sensing region is critical to achieving the ultrafast, accurate, and convenient POCT sensing of EVs for personalized AD diagnosis. Acoustofluidics integrate acoustic waves and microfluidics for handling micro- to nano-scale bioparticles in a versatile, non-contact, label-free manner[15,29–37], highlighting its potential in providing an active means to enrich EVs and enable new POCT sensing systems for early diagnosis and monitoring disease progression of AD.

Here, we develop an integrated POCT sensor (Fig. 1a) for high sensitivity, high speed, and convenience detection of target EVs, highlighting its feasibility for detecting and monitoring the progression of AD. Through the self-aligned acoustoelectric enrichment of EVs, our integrated sensor can (1) enhance the sensitivity and reduce the detection time by pre-concentrating EVs on the sensing area using focused surface acoustic waves and electric pulses, (2) enable the detection of microliter-volume samples through the highly integrated device and microscale footprint of each component, and (3) feature a user-friendly workflow that eliminates the need for specialized operation. Using an AD animal model, we demonstrate the evaluation of AD disease progression, showing an age-dependent Aβ-EV increase in the collected serum profile, showing strong correlations with Aβ plaque loading.

Results

Sensor design and working principle

The integrated POCT sensor consists of an OECT-based sensing unit and an acoustoelectric EV enrichment unit on the same substrate (Fig. 1b). One pair of focused interdigital transducers (F-IDTs) and the source (SE), drain (DE), and gate electrodes (GE) of the OECT sensor were fabricated on the same $LiNbO_3$ substrate through one-time fabrication procedure. The simulation results showed the distributions of acoustic and electric fields (Fig. 1c) for optimizing the integration of the EV enrichment and sensing units. To test the clinical AD EV samples, a sessile droplet of serum sample or EV sample can be added into the spacing ring. Within the sessile droplet, EVs can be actively transported and enriched to the sensing region as the cross-finger electrodes of the OECT sensor under the focused surface acoustic waves (FSAWs) and electric pulses. Then, the target EVs carrying membrane proteins such as Aβ and tau can be selectively captured by the correlated antibodies coated in the sensing region. Once target EVs bind to the sensing region, the relative drain current ($\Delta I_{ds}/I_{ds}(0)$) of the OECT sensor can respond by sensing the number of the target EVs within the AD patient's blood. We expect to detect the number and variation of EVs carrying Aβ or/and tau membrane proteins from an individual AP patient for detecting and monitoring the progression of AD (Fig. 1a). Different from conventional OECT sensing where local EVs randomly and slowly settle down onto the sensing region based on diffusion, the acoustic and electric fields provided an active and rapid means to enrich most of the EVs within the sessile droplet to the sensing region of the OECT sensor. To confirm this, we compared the acoustoelectric enrichment of EVs and the diffusion of EVs by characterizing the EV distribution with and without the FSAWs and electric pluses using scanning electron microscopy (SEM) (Fig. 1d). The acoustoelectric enrichment group (Acou.(+), Elec.(+)) showed the band of heavily enriched EVs, while the diffusion group (Acou.(−), Elec.(−)) showed the sparse and random distributed EVs. Moreover, the EVs in both groups emerged with excellent morphology and intact membranes. Thus, we may demonstrate a new EV-based POCT sensor for personalized diagnosis.

Acoustoelectric enrichment and sensing of EVs

Before testing clinical samples, we validated and tested the acoustoelectric enrichment and sensing of EVs. The polystyrene (PS) particles were trapped into parallel patterns of PS particles within 10 s using FSAWs (Supplementary Fig. 1), highlighting the feasibility of rapid EV enrichment. Customized multiple pairs of electrodes (source and drain) were designed to increase the sensitivity of the OECT sensor. Meanwhile, these electrodes of the OECT sensor were also designed to match the location, gap, and width of the interdigital electrodes for the acoustoelectric EV enrichment, ensuring the enrichment of EVs (or microbeads in Supplementary Fig. 2) to the middle of each pair of electrodes (source and drain). We conducted the enrichment of red fluorescence-labeled EVs of the same concentration at the same time under different enrichment mechanisms including Acou.(+/−), Elec.(+/−) (Fig. 2a). The microscopic images of the region of interest (ROI, red rectangle in the schematics of Fig. 2a) and the quantification of fluorescent intensity distribution (Fig. 2b) of ROI' (white dished rectangle in the image of Fig. 2a) showed that (1) the Acou.(+), Elec.(+/−) groups emerged obvious parallel patterns of EVs while the Acou.(−), Elec.(+/−) groups did not; (2) the Acou.(+/−), Elec.(+) groups enriched more EVs than the Acou.(+/−), Elec.(−) groups, respectively; and (3) the Acou.(+), Elec.(+) group enriched significantly more EVs than the other groups. Thus, the results indicated that the

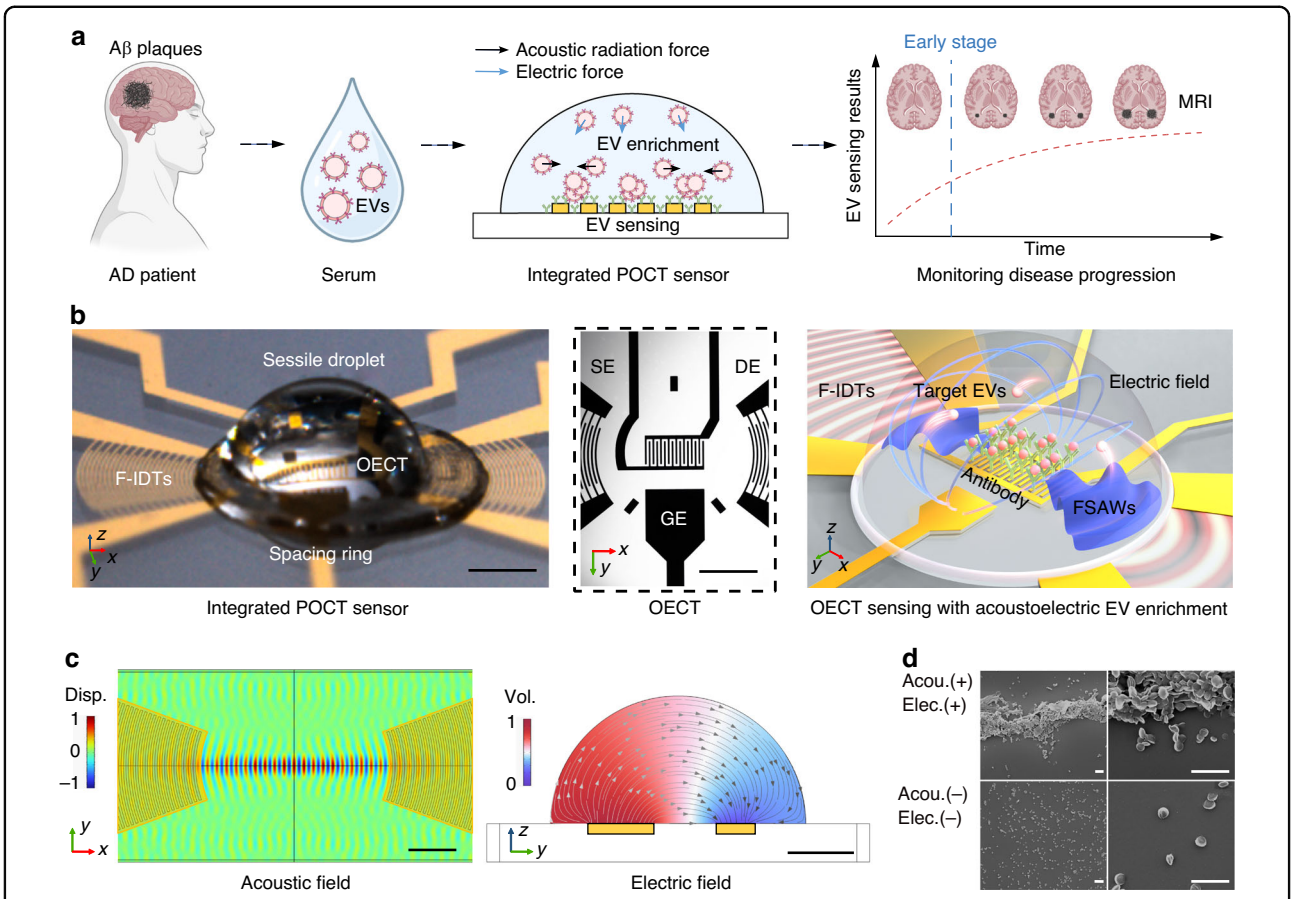

Fig. 1 Point of care testing (POCT) of serum extracellular vesicles (EVs) in Alzheimer's disease (AD). **a** Workflow of an integrated POCT sensor for diagnosis and monitoring progression of AD. **b** Photo of an integrated sensor device with an organic electrochemical transistor (OECT) sensing unit and an acoustoelectric EV enrichment unit (left), and image of the OECT sensor (middle) with source (SE), drain (DE), and gate electrodes (GE), respectively. Scale bar, 500 μm. Working principle of the integrated sensor (right), target EVs can be rapidly enriched using focused surface acoustic waves (FSAWs) and electric pulses and further detected using an OECT coated with correlated antibodies. **c** Simulated distributions of acoustic and electric fields. Scale bar, 500 μm. **d** SEM images of EV distributions with the acoustoelectric enrichment (Acou.(+), Elec.(+)) and conventional condition (Acou.(−), Elec.(−)). Scale bar, 1 μm

simultaneous application of acoustic and electric fields can provide the best enrichment of EVs. The size distribution and concentration of purified EVs were measured by nanoparticle tracking analysis (NTA) and dynamic light scattering (DLS), shown in Supplementary Fig. 3, indicating that the purified EVs possessed the expected size properties. The fluorescence-label EVs were enriched in various conditions (Acou.−/+, Elec.−/+) over 2 min. The surface of OECT was pre-modified by the target antibody. In the Acou.(+), Elec.(−) group (blue rectangle), the focused acoustic field triggers standing waves to enrich EVs into parallel strips; In the Acou.(−), Elec.(+) group (green rectangle), the EVs are attracted by the pulsed electric field; In Acou.(+), Elec.(+) (red rectangle), EVs are enriched under the dual action of the pulsed voltage and acoustic fields and specifically captured. The pattern of enriched EVs under the action of acoustics was highly consistent with the simulation results (Fig. 1c).

Further, we tested the enhanced performance of this acoustoelectric manner on the OECT-based sensing to evaluate the role played by acoustics/electrics. The transfer curve of the processed OECT sensor and the responses for purified EV detection shows a linear response over the operating voltage range (Supplementary Fig. 4). The device performance as a function of accumulated incubation time (Fig. 2c). Herein, the relative drain current ($\Delta I_{ds}/I_{ds}(0)$) was used to describe the responses. During the two-minute incubation, in the blank group (Acou.(−), Elec.(−)), little change was seen in the conversion curve; A tiny response could be seen in the Acou.(−), Elec.(+) group; In the Acou.(+), Elec.(−) group, a rapid rise in the curve was seen, and saturation was reached within two minutes of incubation; In the Acou.(+), Elec.(+) group, the electric field further promoted the enrichment performance of the acoustic field, shortening the saturation time and increasing the

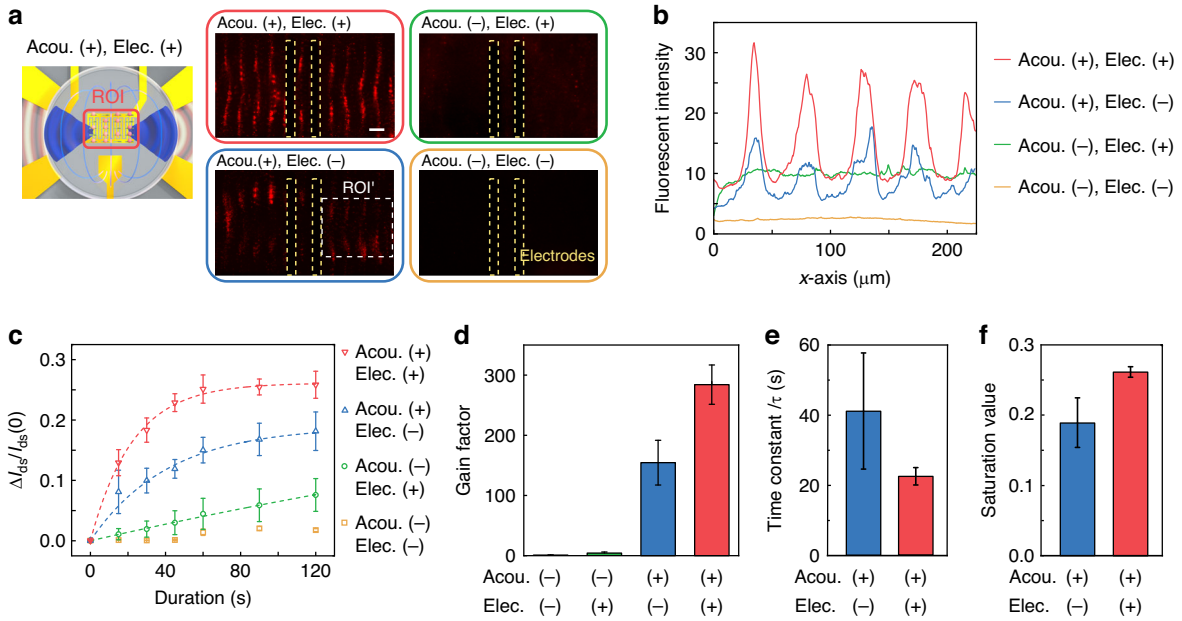

Fig. 2 Acoustoelectric enrichment and sensing of EVs. **a** Schematics and experimental results of EV (red fluorescence-label) enrichment within the region of interest (ROI, red rectangle) under different conditions. Scale bar, 50 μm. **b** Fluorescent intensity of EVs extracted from the ROI' (white dished rectangle). **c** Relative change of the drain current as a function of incubation time under different conditions (mean ± s.e.m., $n = 4$, independent experiments). The dashed curves indicate the response curves fitted using the exponential function. **d** The gain factor of each group with a duration time of 30 s (mean ± s.e.m., $n = 4$, independent experiments). The time constant (**e**) and saturation value (**f**) of the fitting curves in (**c**) (mean ± s.e.m., $n = 4$, independent experiments)

saturation value. The gain factor was used to evaluate the enhancement of the hybrid fields, defined as the relative response ratio (Fig. 2d). At a duration of 30 s, the Acou.(+), Elec.(+) group demonstrated a 284-fold response enhancement compared to passive transport (Acou.(−), Elec.(−)). In addition, the Acou.(−), Elec.(−) group did not show superior enrichment (gain factor = 30 ± 17.9). However, when it superimposed acoustic field (Acou.(+), Elec.(+)), there is a huge boost of the response value by 84% compared to the Acou.(+), Elec.(−) group, suggesting that the electric pulses contribute mainly to the transportation, whereas the acoustic field contributes to the trapping. Further, the relationship can be fitted with an exponential function $\Delta I_{ds}/I_{ds}(0) = A[1 - \exp(-\frac{t}{\tau})]$, where τ is the time constant, which represents the time required to rise to a saturation value of 63.2%, and A is the saturation value. The τ of the Acou.(+), Elec.(+) group and the Acou.(+), Elec. (−) group is 22.4 s and 41.2 s, showing electric pulses reduce the incubation time of the acoustic field by about 50% (Fig. 2e). Moreover, the saturation value also increased from 18.94% to 26.13% (Fig. 2f). It is worth to note that the sensor can complete saturation adsorption of EVs in less than 2 min, which makes the device well-suited for rapid readouts in POCT.

AD diagnosis using serum EV samples

After optimizing the integrated sensor, we further applied the sensor for AD diagnosis using clinical serum samples. We tested different concentrations of serum from AD patients with a 2-min incubation time to calculate the limit of detection (LOD) (Fig. 3a), showing an excellent LOD (calculated as 3 × standard deviation of the baseline (PBS)) of 0.53×10^3 /mL and a limit of quantification (LOQ) of 2.028×10^5 /mL. To harness the high sensitivity of the sensing system and reduce the impact of the individual patient difference, we directly diluted a minimal volume of serum samples that can be collected from the fingertip. To optimize the dilution factor, we tested the serum response from AD patients at different dilutions with/without modified antibodies to find the optimal dilutions (Supplementary Fig. 5a). We defined the response of the unmodified device as the noise due to the unspecific binding and the response of the modified device as the signal. Thus, the signal-to-noise ratio (SNR) is defined by the response ratio between the device with/without modification (Supplementary Fig. 5b). Considering the response value and SNR, we chose the 10^{12} times as the sample pretreatment parameter for the subsequent experiments. To evaluate the specificity of the

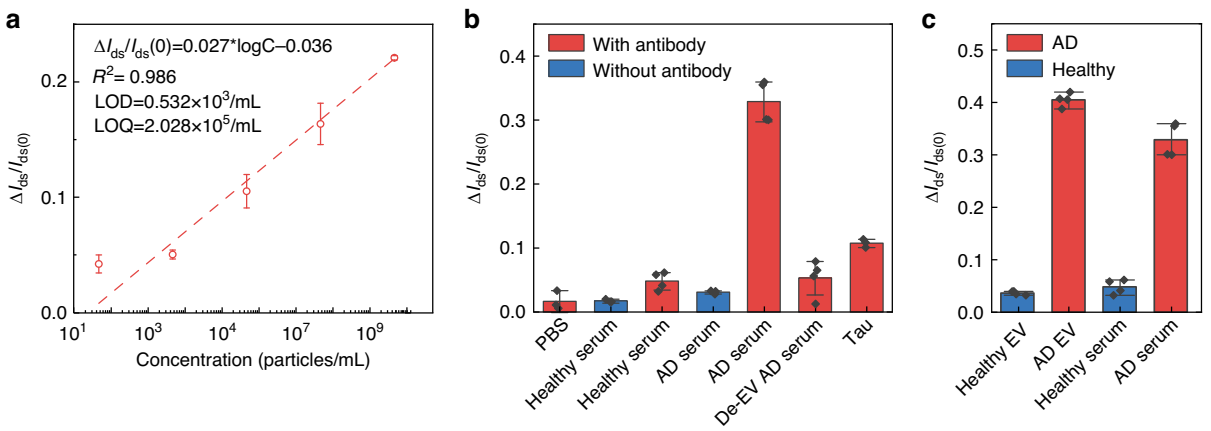

Fig. 3 Detection of serum EVs from AD patients using integrated POCT sensors. **a** Sensitivity of detecting tau EVs from AD serum (mean ± s.e.m., $n = 3$, independent experiments; LOD and LOQ indicate the limit of detection and quantitation, respectively). **b** Sensing results for AD serum from AD patients, health donors, EV-depleted serum, and PBS buffer, indicating the good specificity of the integrated POCT sensors (mean ± s.e.m., $n = 3$ or 4, independent experiments). **c** AD diagnosis based on serum from patients. The sensing results for purified EVs and serum from health donors and AD patients (mean ± s.e.m., $n = 4$, independent experiments)

integrated sensor, serum samples from AD patients ($n = 3$) and healthy individuals ($n = 3$) were divided into two parts, one for EV purification by a commercial kit to obtain EVs in a PBS buffer before detection and the other for detection directly after dilution. Using an incubation time of 2 min, the relative changes of drain current were obtained under different conditions (Fig. 3b). There were two variables: whether or not the surface of the device was modified with an antibody (Positive: with antibody, Negative: without antibody) and whether or not the sample contained EVs from AD patients (Positive: AD serum, Negative: Healthy serum and De-EV AD serum as AD patient serum after removal of EVs). The results showed a significant response from the group with modified antibodies and EVs in the sample, indicating that our technique possesses excellent specificity. The approach was further applied for testing clinical samples (Fig. 3c). The relative changes in the transfer curve in the patient samples were much greater than that in healthy individuals. The results of purified EVs were consistent with those of diluted clinical samples, indicating that the sensor can rapidly identify healthy individuals and patients to achieve AD diagnosis. In addition, the ultra-fast detection speed is a key feature of the device. Compared to the conventional OECT sensor requiring an incubation time of more than 20 min, our approach can reach saturation in only 2 min, showing a significant breakthrough for OECT sensing.

Monitoring disease progression of AD in an animal model

We further investigated the feasibility of applying the integrated sensor to monitor the progression of AD in a well-established 5xFAD mouse model. The 5xFAD mice overexpress human AD-linked mutations including APP and PSEN1 transgenes. After 2 months of age, these mice rapidly develop amyloid pathology characterized by the accumulation of high levels of Aβ42. As a result, the 5xFAD mice display progressive neuronal loss and cognitive and motor deficiencies[38–40]. For our experimental workflow (Fig. 4a), the 5xFAD mice were sacrificed in different age groups (4, 12, and 18 months), with wild-type mice (WT) as the control group. After serum collection and perfusion, the whole brain was fixed. The serum samples were diluted and tested using integrated sensor chips modified with anti-Aβ42. High-resolution MRI, widely used for identifying plague deposition in the brain[41,42], was performed to quantify the age-dependent beta-amyloid loading in each matching brain. Throughout the pathological progression, as shown by the comparison between age groups, there was a significant increase in beta-amyloid loading (MRI results, Fig. 4b, c) as well as detected Aβ42 + EV (sensor readouts, Fig. 4d). For integrated sensor, additional WT serums collected from age matching pairs were tested. The corresponding responses were within the healthy baseline level (<0.05) (Supplementary Fig. 6). In the scatter plot representing the pooled data of all 5xFAD mice, we observed a powerful correlation (Pearson $r = 0.920$) between the integrated sensor measurement ($\Delta I_{ds}/I_{ds}(0)$) and MRI plaque loading (Fig. 4e), which suggests that the integrated sensor could be an effective alternative tool of monitoring AD processes. As the role of exosomal Aβ has been extensively studied and explored during the last decade[43–47], this proof-of-concept study demonstrated that our integrated POCT sensing system can be applied to

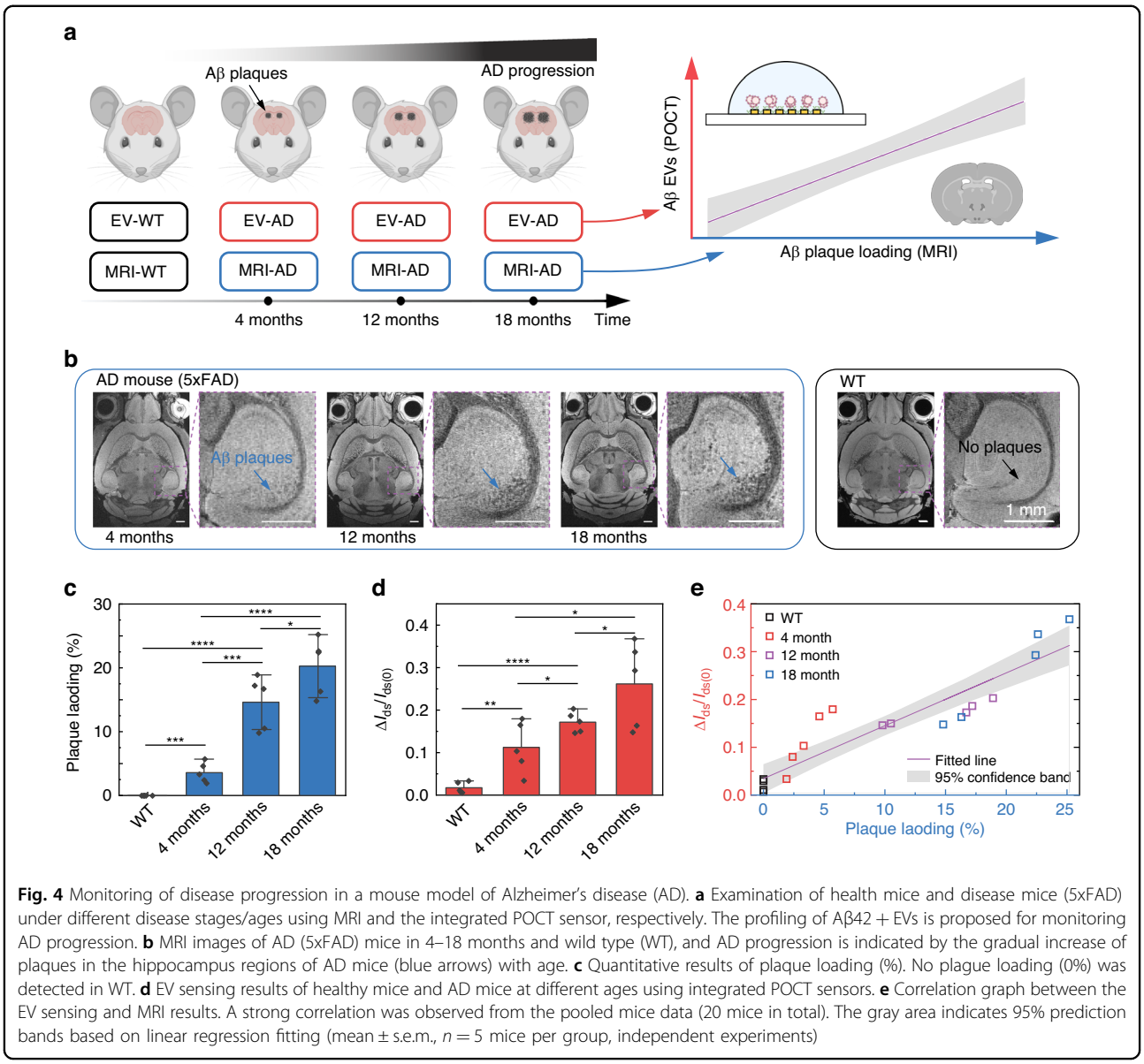

Fig. 4 Monitoring of disease progression in a mouse model of Alzheimer's disease (AD). **a** Examination of health mice and disease mice (5xFAD) under different disease stages/ages using MRI and the integrated POCT sensor, respectively. The profiling of Aβ42 + EVs is proposed for monitoring AD progression. **b** MRI images of AD (5xFAD) mice in 4–18 months and wild type (WT), and AD progression is indicated by the gradual increase of plaques in the hippocampus regions of AD mice (blue arrows) with age. **c** Quantitative results of plaque loading (%). No plague loading (0%) was detected in WT. **d** EV sensing results of healthy mice and AD mice at different ages using integrated POCT sensors. **e** Correlation graph between the EV sensing and MRI results. A strong correlation was observed from the pooled mice data (20 mice in total). The gray area indicates 95% prediction bands based on linear regression fitting (mean ± s.e.m., $n = 5$ mice per group, independent experiments)

enable the diagnosis & prognosis of AD rapidly and minimally invasively.

Discussion

We have demonstrated an integrated POCT sensor that enhanced the performance of the OECT-based sensing by introducing a hybrid active field, achieving AD diagnostics and progress monitoring. This device exploits the powerful transport of electric fields, excellent enrichment of FSAWs, and excellent sensitivity of OECT to construct an ultrafast, highly sensitive, simple-to-operate manner. Compared to the passive transport mode of the classic OECT, this hybrid active transport greatly improves transport efficiency and specifically enriches EVs in the sensing area, increasing nearly 300-fold in response within thirty seconds and decreasing the LOD to hundreds of particles per milliliter. Based on these, we realize rapid AD detection and process monitoring within two minutes.

The system integration, operating procedures, and functionality of the integrated POCT sensor can be improved. Although the devices are millimeter-scale packages that meet the needs of POCT, the exogenous equipment (signal generators and power amplifiers) is not miniaturized and highly integrated. Although achieving successful detection of serum EVs from AD patients, it still needs the involvement of pipetting samples. Additional efforts could be made to incorporate microfluidic modules and automation units for the dilution, mixing, and pumping of various sample fluids for achieving a sample-in-answer-out assay[48]. Moreover, as a versatile

enrichment tool, the acoustoelectric enrichment field has a wide range of compatibility with various interfacial sensing technologies, which can improve the performance and functionality, such as enzyme-linked immunosorbent assay (ELISA)[49], surface plasmon resonance (SPR)[50], and Raman sensing[51], greatly expanding the range of practical applications. In addition, we validated the feasibility of our POCT sensor for AD detection using patient serum samples (Fig. 3b, c) and its potential for monitoring disease progression using a mouse model of AD (Fig. 4). However, additional experiments will still be needed to test the serum samples from AD patients at different stages for fully exploring the potential of our POCT sensor for early diagnosis and progress monitoring of AD. The EV-based POCT sensors hold tremendous potential for personalized medicine because EVs carry a wealth of information that responds to the physiological state of the body, not just the brain[52–54]. Thus, our integrated POCT sensor can be applied to the rapid diagnosis and process monitoring of various diseases by changing the modified antibodies on the substrate. In addition, this ultra-fast and highly sensitive sensor, which requires only a microliter sample, is ideally suited for evaluating and monitoring treatment response[55]. Moreover, by further integrating offline assays such as sequencing, mass spectrometry, etc., the enriched EVs can be further analyzed using multi-omics approaches, which could help discover new biomarkers and reveal disease mechanisms.

Materials and methods

Sensor fabrication

The electrodes of OCET and F-IDTs were fabricated on $LiNbO_3$ substrate (500 µm thick, double-side polished, 128° YX-propagation) using a standard thermal evaporation and liftoff process[56,57]. One pair of F-IDTs was designed with 16 pairs of finger electrodes with the same finger width and gap ($\lambda/4 = 25$ µm) and a 40° focusing angle. The source-drain of the OECT was designed at the focus point patterned as 8 pairs of interdigitated fingers. The length and width of the finger were designed as 325 µm × 25 µm, and the distance between the organic channel and the side gate electrode was designed as 250 µm. The poly(3,4-ethylenedioxythiophene): poly(-styrene sulfonate) (PEDOT: PSS) aqueous solution was doped with divinyl sulfone (5%), (3-glycidyloxypropyl), trimethoxysilane (GOPS, 2%), and ethylene glycol (5%) to improve the conductivity and stability of the organic layer[58–60]. Then, to clean the organic channel before the biofunctionalization, the device was washed with 100% EtOH, air-dried, treated with oxygen plasma for 3 min, and incubated with 2% GOPS solution overnight. The device was washed again with 100% EtOH and dried in the oven at 80 °C for 4 h, then conjugated with antibodies at 4 °C overnight. Anti-Aβ42 (288885, Biolegend, US) and anti-Tau Pho (846601, Biolegend, US) were diluted in 1× PBS and utilized for diagnostics of mouse and human samples, respectively. 5% BSA was used to block the unspecific binding sites for 30 min and kept in the fridge (4 °C) upon usage. Between each step after the antibody conjugation, the device was thoroughly rinsed with 1× PBS three times.

Preparation of AD patient blood samples

The Indiana Biobank, a part of the Indiana Clinical and Translational Sciences Institute (CTSI), provided whole blood samples from AD patients. Serum was collected by density centrifugation, and the EVs were isolated with a commercially available precipitation kit (ExoQuick, System Biosciences, Palo Alto, CA, US) following the protocol provided by the vendor. The freshly isolated EVs were re-suspended in 1× PBS with different dilution factors for further analysis.

Device characterization

The acoustofluidic EV focusing was driven by a function generator (TGP3152, Aim TTi, UK) providing a continuous sine RF signal of ~37.4 MHz and an amplifier (LZY-22+, Mini-circuit, USA). The acoustic enrichment was visualized using fluorescent polystyrene beads (Bangs Laboratories Inc, FSDG005 dragon green, Fishers, IN, USA) diluted in 1× PBS and monitored with an inverted microscope (IX-81, Olympus, Japan). The intensity of the focused beads was quantified in ImageJ. For EV-based characterization, the freshly isolated EV solution was incubated with 50 µg/mL Dil (D282, ThermoFisher, US) for 30 min at 4 °C, and the isolation process was repeated to remove the free dye. The transfer characteristics of the OECT were measured with two source-meter units (Keithley 2612B) with custom control software. The detection area was rinsed with 1× PBS three times between each step. The transfer curve was taken with gate voltage $V_G = -1$V to 1V and $V_{ds} = -0.1$ V. The relative change of the drain current ($\Delta I_{ds}/I_{ds}(0)$) was calculated between the enriched detection ($I_{ds}(1)$) of EVs and the baseline ($I_{ds}(0)$) (1× PBS) by $\Delta I_{ds}/I_{ds}(0) = (I_{ds}(1) - I_{ds}(0))/I_{ds}(0)$. The gain factor is defied by the relative response of the drain current, calculated by the ratio of the enriching group (Acou.(+/−), Elec.(+/−)) and the control group ((Acou.(−), Elec.(−)).

Quantification of EV size and concentration

The EV samples were further quantified with dynamic light scatter (DLS, Zetasizer Nano-S, Malvern) and nanoparticle tracking analyzer (NTA, Zetaview, Particle Metrix). For the DLS, the diluted samples (100 µL) were loaded into a quartz cuvette (zen 2112) to quantify the intensity particle size distribution (PSD). Each measurement was repeated three times with 12 runs per measurement. The system was pre-calibrated with 100 nm

beads for the NTA, and then auto alignment and focus optimization were performed according to the user manual. A 1 ml sample solution was injected into the flow cell, and the size distribution measurement was carried out with the minimum brightness set at 20 and the sensitivity set between 70 and 80.

Scanning electron microscopy (SEM)

Freshly isolated EVs were vortexed and resuspended in 1× PBS at 5×10^5 particles/ml. 2.5 µL of the EV solution was loaded onto the device focus area. After the enrichment, the surface of the device was washed with 1× PBS 10 times and fixed in 3% paraformaldehyde solution for 30 min. The samples were then washed with DI water 10 times, serially dehydrated with 30%, 50%, 70%, and 100% ethanol (15 min each), and air-dried for another 30 min under a ventilation hood. To make the sample surface conductive, a 5 nm gold-palladium alloy coating was sputtered with argon as gas for plasma (Denton Desktop V sample preparation system). The SEM images were taken with a field emission scanning electron microscope (FEI Quanta 600).

Characterization of acoustoelectric enrichment

The purified EVs with a concentration of 4.6×10^7/mL were dripped on the sensing area for a certain period (2 min) for incubation with/without acoustic field (frequency: 37.4 MHz, amplitude: 17 V_{pp}) and with/without voltage pulse (frequency, 10 kHz; voltage, −0.5 V; pulse width, ten µs), and then, the transfer curve of the OECT was measured in PBS buffer after washing three times. This process on the same device was repeated several times with different incubation times (Fig. 2c).

Simulation model

A three-dimensional numerical model was used to visualize the pattern of SAWs on the surface and a two-dimensional model was used to show the electric field in a sessile droplet with COMSOL. For the distribution of the acoustic field, The electrostatics module, solid mechanics module, and multiphysics module (piezoelectric effect) were used. 16 pairs of IDTs with a focused angle of 40° were distributed on the surface of the lithium niobate substrate with a width and spacing of 25 µm, as shown in Fig. 1c. In addition to the symmetric interface, the interface was set as a perfect match layer to represent the infinity boundary, and the bottom interface was set as a fixed constraint. To simulate the electric field, an electrostatics module was used. The SE and DE were set as ground and the GE were set as −0.5 V. The geometry of the sessile droplet was a semicircle with a radius of 1000 µm and the material was water.

Animal preparation

Animal experiments were carried out in compliance with the Indiana University Institutional Animal Care and Use Committee. Four wild-type mice at 12 months and five 5xFAD mice at the ages of 4, 12, and 18 months were sacrificed and perfused with the PBS solution. The mouse brains were immersed in buffered formalin for 24 h and then placed in a PBS solution of 0.5% Prohance (Bracco Diagnostics Inc., Princeton, NJ) to shorten T1 and reduce scan time[42].

MRI protocol

The MRI of the specimens was acquired on a 30-cm bore 9.4 T magnet (Bruker BioSpec 94/30, Billerica, MA) with a maximum gradient strength of 660 mT/m on each axis. A high-sensitivity cryogenic RF surface receive-only coil was used for signal reception (Bruker CryoProbe). A 3D gradient echo (GRE) pulse sequence was performed at the spatial resolution 18 μm^3 with two TEs (10 and 24.5 ms)[41]. The matrix size is $900 \times 640 \times 420$. All other parameters were kept the same: FOV = $16.2 \times 11.52 \times 7.56\ mm^3$, flip angle = 45°, bandwidth (BW) = 125 kHz, average = 2, and TR = 100 ms. The scan time was about 16 h.

Statistical analysis

The statistics comparing different groups were conducted using the *t*-test. Statistical significance was as follows: $^*p < 0.05$, $^{**}p < 0.01$, $^{***}p < 0.005$. $^{****}p < 0.001$.

Acknowledgements

F.G. acknowledges the National Institute of Health Awards (R01DK133864, DP2AI160242, and U01DA056242).

Author details

[1]Department of Intelligent Systems Engineering, Indiana University, Bloomington, IN 47405, USA. [2]Advanced Imaging Research Center, University of Texas Southwestern Medical Center, Dallas, TX 75390, USA. [3]Department of Medicine, Brigham and Women's Hospital, Harvard Medical School, Boston, MA 02115, USA. [4]Department of Mechanical and Aerospace Engineering, and Department of Surgery, University of California San Diego, La Jolla, CA 92093, USA. [5]Department of Bioengineering, and Department of Electrical Engineering and Computer Science, University of California at Berkeley, Berkeley, CA 94720, USA. [6]Institute of Quantum Biophysics, Department of Biophysics, Sungkyunkwan University, Suwon, Korea. [7]Department of Chemistry and Nanoscience, Ewha Womans University, Seoul, Korea

Conflict of interest

The authors declare no competing interests.

Supplementary information The online version contains supplementary material available at https://doi.org/10.1038/s41378-025-00916-4.

Received: 20 June 2024 Revised: 15 November 2024 Accepted: 11 December 2024
Published online: 17 April 2025

References

1. Scheltens, P. et al. Alzheimer's disease. *Lancet* **397**, 1577–1590 (2021).
2. Karran, E. & De Strooper, B. The amyloid hypothesis in Alzheimer disease: new insights from new therapeutics. *Nat. Rev. Drug Discov.* **21**, 306–318 (2022).
3. Aharon, A. et al. Extracellular vesicles of Alzheimer's disease patients as a biomarker for disease progression. *Mol. Neurobiol.* **57**, 4156–4169 (2020).
4. Thijssen, E. H. & Rabinovici, G. D. Rapid progress toward reliable blood tests for Alzheimer disease. *JAMA Neurol.* **78**, 143–145 (2021).
5. Lim, C. Z. J. et al. Subtyping of circulating exosome-bound amyloid beta reflects brain plaque deposition. *Nat. Commun.* **10**, 1144 (2019).
6. Mustapic, M. et al. Plasma extracellular vesicles enriched for neuronal origin: a potential window into brain pathologic processes. *Front. Neurosci.* **11**, 278 (2017).
7. van Niel, G. et al. Challenges and directions in studying cell-cell communication by extracellular vesicles. *Nat. Rev. Mol. Cell Biol.* **23**, 369–382 (2022).
8. Su, L. et al. Identification of altered exosomal microRNAs and mRNAs in Alzheimer's disease. *Ageing Res. Rev.* **73**, 101497 (2022).
9. Zhang, T. et al. The emerging role of exosomes in Alzheimer's disease. *Ageing Res. Rev.* **68**, 101321 (2021).
10. Song, Z. et al. Brain derived exosomes are a double-edged sword in Alzheimer's disease. *Front. Mol. Neurosci.* **13**, 79 (2020).
11. Hamlett, E. D. et al. Neuronal exosomes reveal Alzheimer's disease biomarkers in Down syndrome. *Alzheimers Dement.* **13**, 541–549 (2017).
12. Lin, B. et al. Microfluidic-based exosome analysis for liquid biopsy. *Small Methods* **5** https://doi.org/10.1002/smtd.202001131 (2021).
13. Zhang, P. et al. Ultrasensitive detection of circulating exosomes with a 3D-nanopatterned microfluidic chip. *Nat. Biomed. Eng.* **3**, 438–451 (2019).
14. Im, H. et al. Label-free detection and molecular profiling of exosomes with a nano-plasmonic sensor. *Nat. Biotechnol.* **32**, 490–495 (2014).
15. Chen, Y. et al. Exosome detection via the ultrafast-isolation system: EXODUS. *Nat. Methods* **18**, 212–218 (2021).
16. Liu, C. et al. Low-cost thermophoretic profiling of extracellular-vesicle surface proteins for the early detection and classification of cancers. *Nat. Biomed. Eng.* **3**, 183–193 (2019).
17. Ibsen, S. D. et al. Rapid isolation and detection of exosomes and associated biomarkers from plasma. *ACS Nano* **11**, 6641–6651 (2017).
18. Liu, Y. et al. Enhanced detection in droplet microfluidics by acoustic vortex modulation of particle rings and particle clusters via asymmetric propagation of surface acoustic waves. *Biosensors (Basel)* **12** https://doi.org/10.3390/bios12060399 (2022).
19. Liu, H. et al. Ultrafast, sensitive, and portable detection of COVID-19 IgG using flexible organic electrochemical transistors. *Sci. Adv.* **7**, eabg8387 (2021).
20. Guo, K. et al. Rapid single-molecule detection of COVID-19 and MERS antigens via nanobody-functionalized organic electrochemical transistors. *Nat. Biomed. Eng.* **5**, 666–677 (2021).
21. Khodagholy, D. et al. High transconductance organic electrochemical transistors. *Nat. Commun.* **4**, 2133 (2013).
22. Minamiki, T., Hashima, Y., Sasaki, Y. & Minami, T. An electrolyte-gated polythiophene transistor for the detection of biogenic amines in water. *Chem. Commun.* **54**, 6907–6910 (2018).
23. Hempel, F. et al. PEDOT:PSS organic electrochemical transistors for electrical cell-substrate impedance sensing down to single cells. *Biosens. Bioelectron.* **180**, 113101 (2021).
24. Strakosas, X., Bongo, M. & Owens, R. M. The organic electrochemical transistor for biological applications. *J Appl Polym Sci* **132** https://doi.org/10.1002/app.41735 (2015).
25. Jeong, S. et al. Integrated Magneto-Electrochemical Sensor for Exosome Analysis. *ACS Nano* **10**, 1802–1809 (2016).
26. Park, J. et al. Integrated Kidney Exosome Analysis for the Detection of Kidney Transplant Rejection. *ACS Nano* **11**, 11041–11046 (2017).
27. Marks, A., Griggs, S., Gasparini, N. & Moser, M. Organic Electrochemical Transistors: An Emerging Technology for Biosensing. *Adv Mater Interfaces* **9** https://doi.org/10.1002/admi.202102039 (2022).
28. Yeo, L. Y., Chang, H.-C., Chan, P. P. Y. & Friend, J. R. Microfluidic Devices for Bioapplications. *Small* **7**, 12–48 (2011).
29. Yang, Y. et al. Self-adaptive virtual microchannel for continuous enrichment and separation of nanoparticles. *Sci. Adv.* **8**, eabn8440 (2022).
30. Zhang, N. et al. Microliter ultrafast centrifuge platform for size-based particle and cell separation and extraction using novel omnidirectional spiral surface acoustic waves. *Lab Chip* **21**, 904–915 (2021).
31. Connacher, W., Orosco, J. & Friend, J. Droplet Ejection at Controlled Angles via Acoustofluidic Jetting. *Phys. Rev. Lett.* **125**, 184504 (2020).
32. Naquin, T. D. et al. Acoustic separation and concentration of exosomes for nucleotide detection: ASCENDx. *Sci. Adv.* **10**, eadm8597 (2024).
33. Gu, Y. et al. Acoustofluidic centrifuge for nanoparticle enrichment and separation. *Sci. Adv.* **7**, eabc0467 (2021).
34. Guo, F. et al. Three-dimensional manipulation of single cells using surface acoustic waves. *Proc. Natl Acad. Sci. Usa.* **113**, 1522–1527 (2016).
35. Guo, F. et al. Controlling cell-cell interactions using surface acoustic waves. *Proc. Natl Acad. Sci. Usa.* **112**, 43–48 (2015).
36. Lee, K., Shao, H., Weissleder, R. & Lee, H. Acoustic purification of extracellular microvesicles. *ACS Nano* **9**, 2321–2327 (2015).
37. Pan, S. et al. Biofouling removal and protein detection using a hypersonic resonator. *ACS Sens* **2**, 1175–1183 (2017).
38. Oblak, A. L. et al. Comprehensive evaluation of the 5XFAD mouse model for preclinical testing applications: a MODEL-AD study. *Front Aging Neurosci.* **13**, 713726 (2021).
39. Forner, S. et al. Systematic phenotyping and characterization of the 5xFAD mouse model of Alzheimer's disease. *Sci. Data* **8**, 270 (2021).
40. Medina-Vera, D. et al. Transcending the amyloid-beta dominance paradigm in Alzheimer's disease: An exploration of behavioural, metabolic, and gut microbiota phenotypes in 5xFAD mice. *Neurobiol. Dis.* **187**, 106295 (2023).
41. Wang, N. et al. Accelerating quantitative susceptibility imaging acquisition using compressed sensing. *Phys. Med Biol.* **63**, 245002 (2018).
42. Wang, N. et al. Neurite orientation dispersion and density imaging of mouse brain microstructure. *Brain Struct. Funct.* **224**, 1797–1813 (2019).
43. Dinkins, M. B., Dasgupta, S., Wang, G. H., Zhu, G. & Bieberich, E. Exosome reduction in vivo is associated with lower amyloid plaque load in the 5XFAD mouse model of Alzheimer's disease. *Neurobiol. Aging* **35**, 1792–1800 (2014).
44. Sardar Sinha, M. et al. Alzheimer's disease pathology propagation by exosomes containing toxic amyloid-beta oligomers. *Acta Neuropathol.* **136**, 41–56 (2018).
45. Ruan, J., Miao, X., Schluter, D., Lin, L. & Wang, X. Extracellular vesicles in neuroinflammation: Pathogenesis, diagnosis, and therapy. *Mol. Ther.* **29**, 1946–1957 (2021).
46. Rufo, J., Cai, F. Y., Friend, J., Wiklund, M. & Huang, T. J. Acoustofluidics for biomedical applications. *Nat Rev Method Prime* **2** https://doi.org/10.1038/s43586-022-00109.7 (2022).
47. Rajendran, L. et al. Alzheimer's disease beta-amyloid peptides are released in association with exosomes. *Proc. Natl Acad. Sci. USA* **103**, 11172–11177 (2006).
48. Sackmann, E. K., Fulton, A. L. & Beebe, D. J. The present and future role of microfluidics in biomedical research. *Nature* **507**, 181–189 (2014).
49. Zhang, L. et al. Surface acoustic wave-driven enhancement of enzyme-linked immunosorbent assays: ELISAW. *Anal. Chem.* https://doi.org/10.1021/acs.analchem.4c01615 (2024).
50. Renaudin, A., Chabot, V., Grondin, E., Aimez, V. & Charette, P. G. Integrated active mixing and biosensing using surface acoustic waves (SAW) and surface plasmon resonance (SPR) on a common substrate. *Lab Chip* **10**, 111–115 (2010).
51. Nitta, N. et al. Raman image-activated cell sorting. *Nat. Commun.* **11**, 3452 (2020).
52. Min, L. et al. Advanced nanotechnologies for extracellular vesicle-based liquid biopsy. *Adv., Sci., (Weinh.)* **8**, e2102789 (2021).
53. Yu, D. et al. Exosomes as a new frontier of cancer liquid biopsy. *Mol. Cancer* **21**, 56 (2022).
54. Zheng, W. et al. Diagnosis of paediatric tuberculosis by optically detecting two virulence factors on extracellular vesicles in blood samples. *Nat. Biomed. Eng.* **6**, 979–991 (2022).
55. Zhang, K. & Cheng, K. Stem cell-derived exosome versus stem cell therapy. *Nat. Rev. Bioeng.* 1–2 https://doi.org/10.1038/s44222-023-00064-2 (2023).
56. Cai, H. et al. Profiling cell-matrix adhesion using digitalized acoustic streaming. *Anal. Chem.* **92**, 2283–2290 (2020).
57. Lenshof, A., Evander, M., Laurell, T. & Nilsson, J. Acoustofluidics 5: building microfluidic acoustic resonators. *Lab Chip* **12**, 684–695 (2012).
58. Mantione, D. et al. Low-temperature cross-linking of PEDOT:PSS films using divinylsulfone. *ACS Appl. Mater. Interfaces* **9**, 18254–18262 (2017).
59. Håkansson, A. et al. Effect of (3-Glycidyloxypropyl)Trimethoxysilane (GOPS) on the electrical properties of PEDOT:PSS Films. *J. Polym. Sci. Pol. Phys.* **55**, 814–820 (2017).
60. Pasha, A., Khasim, S., Al-Hartomy, O. A., Lakshmi, M. & Manjunatha, K. G. Highly sensitive ethylene glycol-doped PEDOT-PSS organic thin films for LPG sensing. *RSC Adv.* **8**, 18074–18083 (2018).